frontiers | Frontiers in Energy Research

TYPE Original Research
PUBLISHED 09 June 2025
DOI 10.3389/fenrg.2025.1579855

OPEN ACCESS

EDITED BY
Nanda Kishore,
Indian Institute of Technology Guwahati, India

REVIEWED BY
Shansi Tian,
Northeast Petroleum University, China
Nanhang Dong,
Northeast Electric Power University, China

*CORRESPONDENCE
Lei Deng,
leideng@mail.xjtu.edu.cn

RECEIVED 24 February 2025
ACCEPTED 27 May 2025
PUBLISHED 09 June 2025

CITATION
Wu Q, Fang F, Guan J, Zhu L, Chen Y and Deng L (2025) Numerical study on retrofitting opposed firing boilers with a slag-tap combustion chamber.
Front. Energy Res. 13:1579855.
doi: 10.3389/fenrg.2025.1579855

Numerical study on retrofitting opposed firing boilers with a slag-tap combustion chamber

Qinglong Wu[1], Fan Fang[1], Jingyu Guan[2], Lingkun Zhu[2], Yang Chen[3] and Lei Deng[3]*

[1]Xi'an Thermal Power Research Institute Co., Ltd., Xi'an, China, [2]Harbin Boiler Co., Ltd., Harbin, China, [3]State Key Laboratory of Multiphase Flow in Power Engineering, School of Energy and Power Engineering, Xi'an Jiaotong University, Xi'an, China

The utilization of high-alkali coals like Naomaohu coal in conventional opposed firing boilers faces operational challenges due to severe slagging and fouling caused by low ash fusion temperatures and elevated sodium content. This study proposes a cost-effective retrofit design integrating a slag-tap combustion chamber with modular airflow control, preserving the original slag discharge mechanisms of a 350 MW supercritical opposed firing boiler. Three-dimensional numerical modeling based on the Computational Fluid Dynamics (CFD) simulations is conducted to evaluate the flow field, thermal, and gas-phase composi-tional distributions across the Naomaohu coal combustion ratios (20%, 25%, and 30%). The retrofitted configuration enhances slag capture efficiency and reduces fouling risks while maintaining combustion stability. Results demonstrate that elevated combustion ratios intensified the momentum of exhaust jets originating from the slag-tap combustion chamber, generating pronounced flow perturbations within the furnace volume. At the 30% combustion ratio, the jet extends its penetration distance, redistributing pulverized coal particles toward the furnace center and creating distinct thermal zones, including a high-temperature core (~2140 K) and peripheral low-temperature regions (~1600 K). Oxygen depletion in the upper-middle furnace correlates with intensified combustion reactions, while CO_2 accumulation reflects enhanced gas-phase reaction completeness. This study provides critical insights into optimizing combustion systems for high-alkali coals, balancing operational reliability with sustainable energy generation.

KEYWORDS

opposed firing boiler, slag-tap combustion chamber, numerical simulation, highalkali coal, retrofit design, coal combustion ratios

1 Introduction

The global energy landscape is increasingly shaped by the need to balance energy security with environmental sustainability. In regions such as Xinjiang, China, the abundant reserves of high-alkali coals, exemplified by Naomaohu coal, offer a significant energy resource. However, these coals exhibit elevated sodium concentrations coupled with compromised ash thermal stability, creating persistent operational constraints in conventional combustion systems. The inherent physicochemical characteristics induce accelerated ash deposition mechanisms within boiler convective sections,

manifesting as compromised heat exchange efficiency, escalated maintenance cycles, and operational reliability risks (Zhang et al., 2016; Li et al., 2018; Hang et al., 2020; Huang et al., 2021). These challenges have prompted extensive research efforts aimed at investigating the combustion processes and slagging behavior specific to Zhundong coal (Wang et al., 2018; Lei et al., 2019; Jing et al., 2022). Key areas of focus include the interaction of alkali metals and the link between ash fusibility and coal composition, as well as the impact of additives on alkali metal migration and slagging tendencies (Li et al., 2017; Hariana et al., 2023; Zhang et al., 2023). It is widely established that the primary cause of slagging and fouling in Zhundong coal is its elevated sodium levels.

The alkali metals in high-alkali coals exhibit pronounced volatility, with distinct migration behaviors depending on their chemical forms and phase transformations during combustion. The migration of sodium can be categorized into three sequential stages, volatilization release, char combustion, and ash formation, corresponding to the early, intermediate, and final phases of the combustion process, respectively. During combustion, soluble alkali species within coal particles migrate outward via physical or chemical pathways. A fraction of soluble alkali metals volatilizes into the gas phase, while the majority of insoluble alkali compounds remain trapped in residual ash or slag. Notably, temperature critically governs sodium release dynamics (Li et al., 2016). Elevated temperatures enhance the volatilization of sodium-bearing species, which subsequently condense on cooler surfaces or nucleate on ash particles. This gaseous sodium release significantly contributes to ash deposition, a primary factor exacerbating fouling and slagging issues in coal-fired power plants.

Traditional approaches to mitigate these challenges have relied on blending high-alkali coals with low-sodium alternatives (Yang et al., 2019; Yang et al., 2020; Zhang et al., 2020; Huang et al., 2022; Li et al., 2022; Tang et al., 2022; Wang et al., 2022; Meng et al., 2023). This strategy has proven effective in reducing slagging and fouling tendencies, as demonstrated by Yang et al. (2020) and Huang et al. (2022). However, the limited availability of low-sodium coals in Xinjiang and neighboring regions has rendered blending increasingly impractical. Furthermore, the rapid industrial development and growing energy demand in these areas underscore the urgent need for alternative solutions that do not depend on coal blending.

Opposed firing boilers, widely used in coal-fired power plants because of their operational flexibility and relatively straightforward design, face significant challenges when burning high-alkali coals (Zhu J. et al., 2022; Deng et al., 2024; Qi et al., 2024). These coals exhibit reduced ash fusion temperatures and elevated sodium concentrations. Such properties intensify the deposition of slag on furnace surfaces and ash accumulation on heat exchangers, leading to operational inefficiencies and increased maintenance costs. These issues are particularly pronounced in supercritical boilers, where high combustion intensities and temperatures further aggravate slagging and fouling phenomena.

In recent years, slag-tap boilers have emerged as a promising solution for burning slag-prone coals. These boilers are designed to operate at high combustion intensities and effectively capture slag, thereby mitigating slagging and fouling issues (Song and Li, 2022; Wu et al., 2024; Xu, 2024; Zhou et al., 2024). Among these technologies, cyclone combustion has gained attention for its superior slag capture efficiency, significantly reducing the concentration of fly ash in the flue gas exiting the furnace (Wang et al., 2021a; Ni et al., 2022). Additionally, high-temperature liquid slag has demonstrated a strong capability to capture alkali metals, which helps alleviate adhesive ash deposition on heating surfaces. The slag-tap combustion chamber's efficacy in mitigating sodium-related deposition stems from its ability to retain alkali metals within the molten slag phase. At high combustion temperatures (>2000 K), sodium compounds (e.g., NaCl, Na_2SO_4) exhibit increased solubility in silicate-based slag matrices (Shen et al., 2017). The continuous liquid slag layer acts as a dynamic sink, capturing sodium species released during devolatilization and char combustion. Furthermore, the cyclonic flow within the slag-tap chamber prolongs particle residence time, enhancing ash-slag interactions and reducing gas-phase sodium mobility. This mechanism significantly curtails sodium condensation on heating surfaces, addressing a critical limitation of conventional opposed firing systems (Gong et al., 2021). However, despite these advantages, slag-tap boilers face challenges associated with their high operating temperatures, including increased NO_x emissions, greater physical heat loss through slag, and limited flexibility in adjusting boiler loads.

To overcome these challenges, this study introduces an innovative retrofitting strategy for traditional opposed firing boilers by integrating a slag-tap combustion chamber at the furnace rear without modifying the existing combustion and slag discharge systems. Unlike conventional designs that require complete burner replacement, the retrofit introduces a modular combustion chamber that enhances slag capture efficiency without altering the original slag discharge system. This approach uniquely balances combustion stability and retrofit feasibility, addressing a critical gap in high-alkali coal utilization. An industrial-scale 350 MW unit serves as primary case study, with three-dimensional Computational Fluid Dynamics (CFD) modeling analyzing the retrofit's influence on combustion performance and flow behavior within the furnace. The study evaluates how variations in Naomaohu coal blend proportions alter flow dynamics, thermal characteristics, and compositional characteristics across the furnace volume. By incorporating the benefits of slag-tap technology, the retrofitted system aims to enhance slagging resistance, reduce fouling, and improve operational reliability while maintaining the flexibility and scalability of opposed firing configurations. The system's adaptability to various coal blends and alternative low-carbon fuels further reduces the carbon footprint of energy generation. Moreover, maintaining combustion stability and operational efficiency significantly reduce secondary emissions, including unburned carbon, thereby promoting cleaner and more sustainable energy production. These innovations not only advance the decarbonization of coal-fired power generation but also align with global climate objectives, accelerating the transition to a sustainable energy landscape.

2 Boiler configuration and retrofit strategy

This study examines a 350 MW supercritical once-through boiler with a Π-type arrangement, featuring water-cooled walls

TABLE 1 Design parameters of the boiler (BMCR condition).

Parameter	Superheated steam flow rate (t h^{-1})	Superheated steam temperature (K)	Superheated steam pressure (MPa)	Feed water temperature (K)	Reheated steam flow rate (t h^{-1})	Excess air ratio
Value	1158.0	847.0	25.8	567.0	962.0	1.17

TABLE 2 Fuel property analysis of the design coal.

Proximate analysis (%)				Ultimate analysis (%)					$Q_{net,ar}$ (MJ·kg^{-1})
M_{ar}	A_{ar}	V_{daf}	FC_{ar}	C_{ar}	H_{ar}	O_{ar}	N_{ar}	S_{ar}	
17.25	14.72	32.04	35.99	54.31	2.78	9.84	0.56	0.54	19.94

Note: M_{ar} is the moisture content on an as-received basis (%). A_{ar} is the ash content on an as-received basis (%). V_{daf} is the volatile matter on a dry and ash-free basis (%). FC_{ar}, is the fixed carbon on an as-received basis (%). C_{ar} is the carbon content on an as-received basis (%). H_{ar} is the hydrogen content on an as-received basis (%). O_{ar} is the oxygen content on an as-received basis (%). N_{ar} is the nitrogen content on an as-received basis (%). S_{ar} is the sulfur content on an as-received basis (%). $Q_{net,ar}$ is the calorific value on an as-received basis (MJ·kg^{-1}).

that combine spiral and vertical configurations. The combustion chamber of the boiler incorporates four cyclone burners arranged in an opposed-wall firing configuration, with two burners symmetrically installed on both the front and rear furnace walls. This bi-directional burner layout facilitates flame interaction optimization and enhances combustion homogeneity within the reaction zone. To address the limitations of the conventional boiler while preserving its fundamental combustion and slag discharge characteristics, a retrofitting methodology is developed. This involves replacing the burner associated with a coal mill with a slag-tap combustion chamber. The retrofit design includes four single-row burners, which are one-quarter of the number of burners in a double-U slag-tap boiler, maintaining a similar arrangement (Wang et al., 2024; Jing et al., 2022; Yang et al., 2024). The design parameters for the boiler under the Boiler Maximum Continuous Rating (BMCR) condition are provided in Table 1, reflecting typical operational conditions to ensure that the simulations conducted in this study accurately represent real-world scenarios. The coal property analysis of the boiler design coal is summarized in Table 2. Moisture, ash, and volatile matter contents quantified via thermogravimetric drying, ashing, and pyrolysis, respectively. The fixed carbon was derived by mass balance subtraction. Ultimate analysis employed elemental quantification following ASTM D388-19 (International, 2019) or GB/T 5751-2009 (Administration, 2009), with oxygen content resolved stoichiometrically.

In the retrofitted design, the primary and secondary air streams carrying pulverized coal are vertically delivered into the reaction zone for ignition and oxidation processes. The resultant high-temperature combustion products flow via the slag-catching pipes into the furnace chamber, where they continue to release heat. The combustion chamber has a height of 13.934 m (measured to the bottom of the ash hopper), a width of 3.198 m, and a depth of 5.180 m. The furnace chamber is significantly larger, with a height of 39.160 m, a width of 14.048 m, and a depth of 13.970 m. The detailed geometrical structure of the boiler is illustrated in Figure 1.

The detailed structural profile of the cyclone burner is illustrated in Figure 2. Each burner consists of a center air channel, a primary air channel, an inner secondary air channel, and an outer secondary air channel. Pulverized coal is introduced into the furnace chamber through the primary air channel, while both the primary and secondary air channels are equipped with axial cyclone blades to generate cyclonic flow at the burner outlet. The cyclonic directions of the primary and secondary airflows are designed to oppose each other, and the cyclonic directions of adjacent burners are also configured to be opposite. This arrangement enhances mass transfer within the furnace, thereby improving combustion efficiency and heat transfer performance. Figure 3 illustrates the geometric model of the retrofitted opposed firing boiler. In the model construction, a Cartesian coordinate system is adopted, with the origin located on the front wall. The positive direction of the x-axis is defined from the rear wall toward the front wall.

3 Computational modeling

3.1 Mesh development

To balance computational accuracy and efficiency, a non-uniform computational mesh is generated for the boiler through a hybrid meshing strategy. In regions with complex geometries and intense physicochemical interactions (e.g., burners and combustion chamber), a dense hexahedral mesh (cell size ≤0.2 m) is applied to resolve steep gradients in velocity, temperature, and species concentrations. Conversely, the upper cooling chamber, characterized by uniform flow patterns, is discretized with coarser hexahedral elements (cell size ≤0.6 m). Figure 4 illustrates the front and side views of the boiler grid model.

Three mesh configurations with total cell counts of 2 437 861, 3 323 764, and 4 176 259 are tested under BMCR conditions to validate grid independence. The average horizontal gas temperature within the furnace under BMCR conditions for these grid configurations

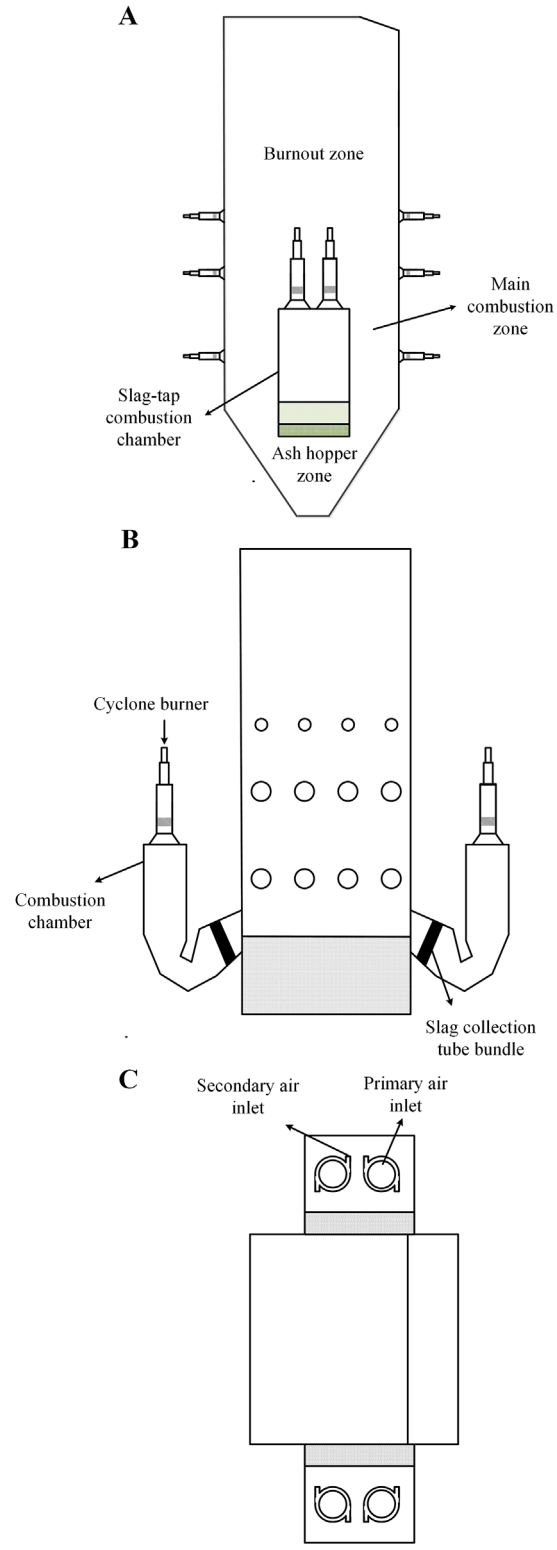

FIGURE 1
Geometry structure of the boiler. **(A)** Front view. **(B)** Side view. **(C)** Top view.

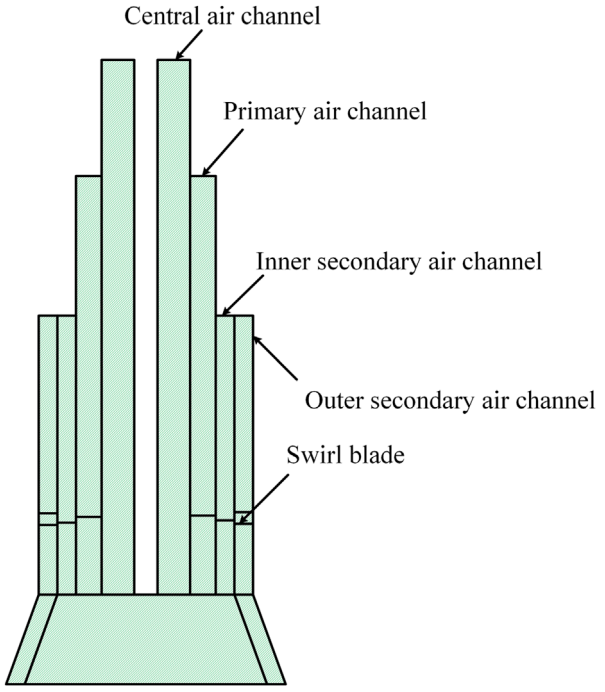

FIGURE 2
The detailed structural profile of the cyclone burner.

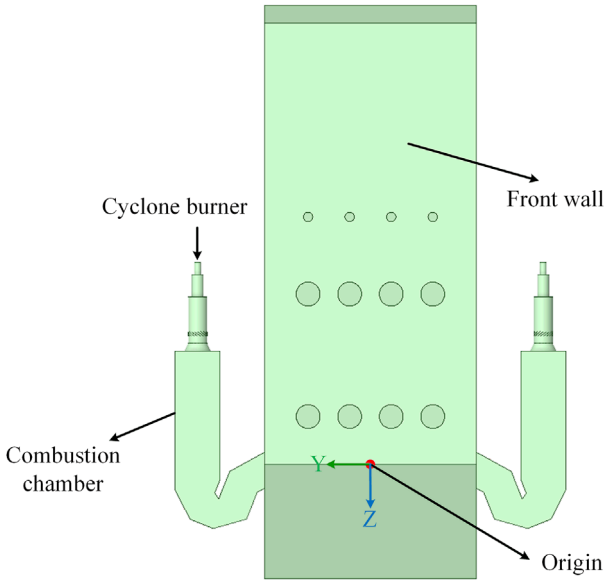

FIGURE 3
Geometric model of the retrofitted boiler.

are shown in Figure 5. When the grid resolution increases from 3 323 764 to 4 176 259 cells, the temperature distribution remained largely unchanged, indicating that further refinement has a negligible

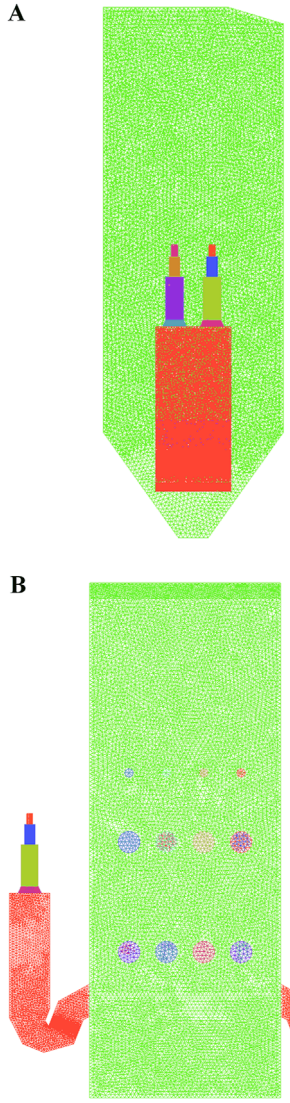

FIGURE 4
Mesh generation. **(A)** Front view. **(B)** Side view.

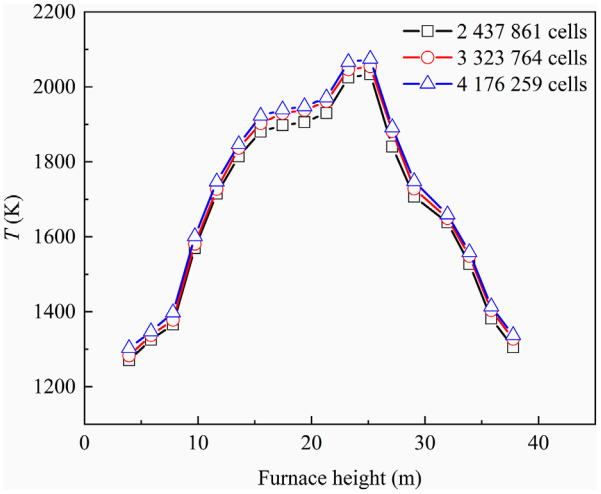

FIGURE 5
Temperature distribution in furnace height direction with different number of grids.

impact on the simulation results. The grid configuration with 3 323 764 cells is therefore adopted for subsequent simulations, achieving optimal balance between predictive fidelity and resource allocation.

3.2 Simulation methodology

This study employs ANSYS Fluent 2020 R2 software for computational analysis. The solver executes discretized conservation equations governing critical thermodynamic parameters (thermal energy, momentum flux, and multi-component transport) across the spatial discretization framework (Rachele et al., 2023). Thermal coupling mechanisms, including convective heat transfer and wall boundary interactions, are resolved through the activated energy conservation formulation. The turbulent momentum transport is addressed via the Realizable k-ε closure with enhanced curvature correction, which ensures accurate predictions for complex flow conditions (Nakamura et al., 2023). The CFD simulations solve the following conservation equations for mass, momentum, energy, and species transport under steady-state conditions as shown in Equations 1–5:

(1) Mass conservation equation.

$$\frac{\partial \rho}{\partial t} + \frac{\partial}{\partial x_i}(\rho u_i) = 0 \tag{1}$$

where ρ denotes the fluid density (kg m^{-3}), and u_i represents the velocity component in the x_i direction (m s^{-1}).

(2) Momentum conservation equation.

$$\frac{\partial}{\partial t}(\rho u_i) + \frac{\partial}{\partial x_i}(\rho u_i u_j) = -\frac{\partial p}{\partial x_i} + \frac{\partial \tau_{ij}}{\partial x_j} + \rho g_i + F_i \tag{2}$$

where p denotes the static pressure (Pa), τ_{ij} represents the stress tensor (N m^{-2}), and g_i and F_i correspond to the gravitational body force and external body force in the i direction (N kg^{-1}), respectively.

The stress tensor is given by the following equation:

$$\tau_{ij} = \left[\mu\left(\frac{\partial u_i}{\partial x_j} + \frac{\partial u_j}{\partial x_i}\right)\right] - \frac{2}{3}\mu\frac{\partial u_l}{\partial x_l}\delta_{ij} \tag{3}$$

(3) Energy conservation equation.

$$\frac{\partial(\rho T)}{\partial t} + div(\rho u T) = div\left(\frac{k}{c_p} grad T\right) + S_T \tag{4}$$

where c_p denotes the specific heat capacity (J kg^{-1} K^{-1}), T denotes the temperature (K), k is the thermal conductivity of the fluid (W m^{-1} K^{-1}), and S_T represents the internal heat source within the fluid and the portion of mechanical energy converted into thermal energy due to viscous effects, often referred to as the viscous dissipation term (W m^{-3}).

TABLE 3 Fuel property analysis of the Naomaohu coal.

Proximate analysis (%)				Ultimate analysis (%)					$Q_{net,ar}$ (MJ·kg^{-1})
M_{ar}	A_{ar}	V_{daf}	FC_{ar}	C_{ar}	H_{ar}	O_{ar}	N_{ar}	S_{ar}	
22.60	11.02	30.15	36.23	50.46	3.32	11.46	0.67	0.47	18.80

TABLE 4 Naomaohu coal combustion ratios under different working conditions.

Working conditions	1	2	3
Naomaohu coal combustion ratios (%)	20	25	30

(4) Component conservation equation.

$$\frac{\partial(\rho c_s)}{\partial t} + div(\rho u c_s) = div(D_S grad(\rho c_s)) + S_S \quad (5)$$

where c_s is the volume concentration (kg m^{-3}), D_S signifies the diffusion coefficient (m^2 s^{-1}), and S_S represents the generation rate (kg m^{-3} s^{-1}).

To enhance computational efficiency and stability, the SIMPLE algorithm is applied for solving the flow field, as it offers faster convergence for relatively simple flow configurations (Zhu B. et al., 2023). Due to the low pressure variation and flow velocity of the flue gas, the pressure-based solver is chosen. The gradient term is discretized using the Green-Gauss Cell-Based method, and the control equations are discretized with the first-order upwind scheme to ensure numerical stability.

For the mass transfer process, the species transport model is utilized, where the physical properties and mass fractions of components are defined within the Mixture model. The finite-rate/eddy dissipation model couples finite-rate Arrhenius kinetics with turbulence-modulated dissipation rates, achieving optimal equilibrium between detailed chemistry and computational tractability (Dugum and Hanjalic, 2019). In comparison, the eddy dissipation concept model resolves microscale combustion events in turbulent dissipation eddies, requiring intensive chemical mechanism integration. The eddy dissipation model presumes turbulent time scales dominate over molecular kinetics, sacrificing chemical fidelity for accelerated computation. Through systematic benchmarking of solution accuracy versus computational overhead, the hybrid kinetic-turbulence methodology is implemented for reactive flow simulations. Considering the balance between computational efficiency and accuracy, the finite-rate/eddy dissipation model is selected for gas-phase reaction simulations.

The numerical calculation process proceeds in two stages. First, the cold flow field within the furnace, excluding pulverized coal particles, is simulated and iteratively solved until convergence is achieved. Once the flow field stabilizes, the Discrete Phase Model is employed to account for the coupling between the discrete phase (pulverized coal particles) and the continuous flow field (Su et al., 2024). The continuous phase is iterated for 30 steps before performing discrete-phase calculations for stable multiphase resolution.

3.3 Thermal calculation methods

In this study, the Standard Method for Thermal Calculation of Boiler Units (Shi et al., 2023) was applied to carry out thermal calculation. The standard treats the combustion chamber, slag trap bundle and cooling chamber as the fundamental units for thermal calculation. From the perspective of thermal balance, the radiative heat transfer and convective heat transfer were calculated separately for these three units, and the flue gas temperature at the outlet of each unit is further calculated. The heat transfer calculation for the combustion chamber is developed based on the heat transfer equation and the heat balance equation, where the heat transfer equation is:

$$Q_f = 5.7 \times 10^{-11} \times \frac{\alpha_{1\cdot ZS} H_f}{B_p}\left(T_\varphi^4 - T_\varepsilon^4\right) \quad (6)$$

$$Q_d = \frac{\alpha_d H_f\left(T_\varphi - T_\varepsilon\right)}{B_p} \times 10^{-3} \quad (7)$$

where Q_f represents the combustion chamber radiation heat transfer (kJ kg^{-1}), $\alpha_{1\cdot ZS}$ denotes the furnace room converted blackness (dimensionless), T_ε is the radiation heating surface wall temperature (K), H_f defines the radiation heating area (m^2), B_p refers to the calculation of fuel consumption (kg s^{-1}), T_φ indicates the effective temperature of the medium in the furnace (K), Q_d defines the convective heat transfer within the combustion chamber (kJ kg^{-1}), and α_d characterizes the convective heat transfer coefficient in the furnace (W m^{-2} K^{-1}).

The heat balance equation is:

$$Q_f + Q_d = \varphi(Q_T - I_T'') \quad (8)$$

where Q_T denotes the effective heat release within the furnace (kJ kg^{-1}), φ represents the heat retention coefficient (dimensionless), and I_T'' corresponds to the enthalpy of combustion products per kilogram of fuel (kJ kg^{-1}), evaluated at the outlet temperature of the combustion chamber or cooling chamber under a specified excess air coefficient α''.

The outlet flue gas temperature of the combustion chamber can be obtained by solving the heat transfer equation and the heat balance equation together. The radiant heat transfer and convective heat transfer between the flue gas

TABLE 5 Comparison of the thermal calculation and numerical results.

Parameter	Thermal calculation results	CFD results
Combustion chamber outlet flue gas temperature (K)	1917.6	1923.8
Slag trap bundle outlet flue gas temperature (K)	1638.7	1646.5
Cooling chamber outlet flue gas temperature (K)	1579.1	1594.6

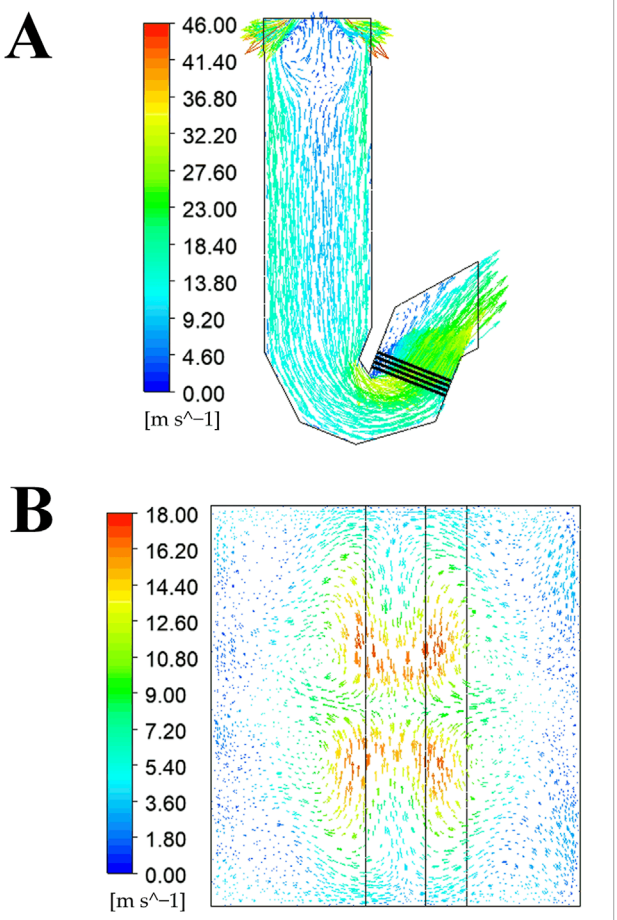

FIGURE 6
Velocity vector distribution in the combustion chamber. **(A)** x = −5.4 m **(B)** z = −5.8 m.

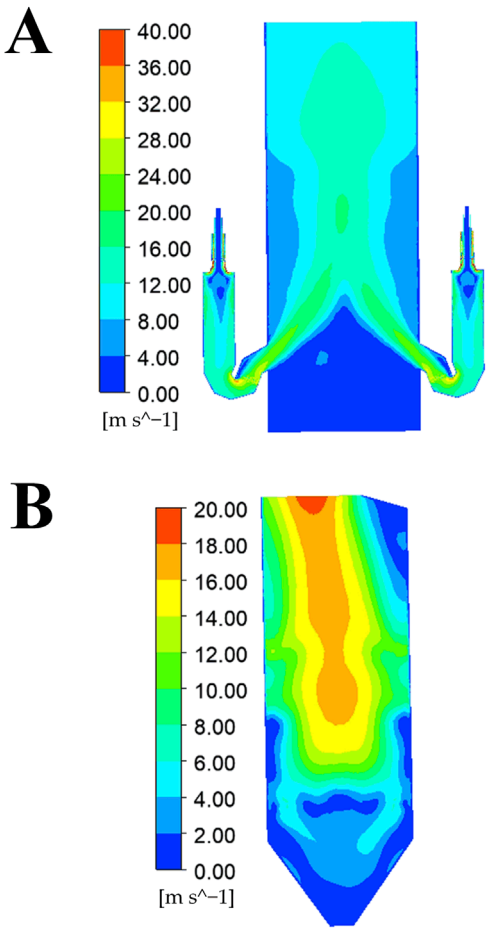

FIGURE 7
Velocity vector distribution in the furnace. **(A)** x = −5.4 m **(B)** y = 0 m.

and the slag trap bundle are calculated according to the following equation:

$$Q_{bz} = \frac{\left(\alpha_d + \alpha_f\right) H\left(\theta_{cp} - T_{zm \cdot bz}\right)}{B_{p \cdot ql}} \times 10^{-3} \quad (9)$$

where α_f represents the radiative heat transfer coefficient (W m^{-2} K^{-1}), H denotes the heat transfer area of the slag trap bundle (m^2), $T_{zm \cdot bz}$ corresponds to the surface temperature of the liquid slag film (K), which is set 100 K lower than the slag film temperature in the combustion chamber, and θ_{cp} defines the average flue gas temperature (K).

In the cooling chamber, radiative heat transfer dominates due to the low flue gas velocity, and convective contributions are negligible. The thermal calculation employs the heat transfer equation (Equation 6) and energy balance equation (Equation 8). The outlet flue gas temperature is determined by simultaneously solving these coupled equations, ensuring consistency between heat exchange mechanisms and thermodynamic equilibrium.

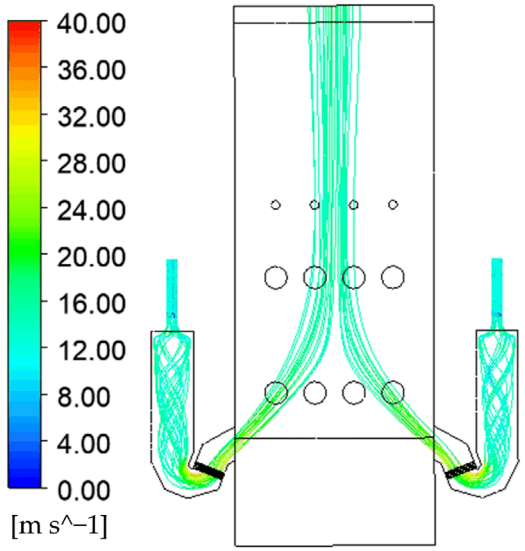

FIGURE 8
The streamlines in the cyclone burner.

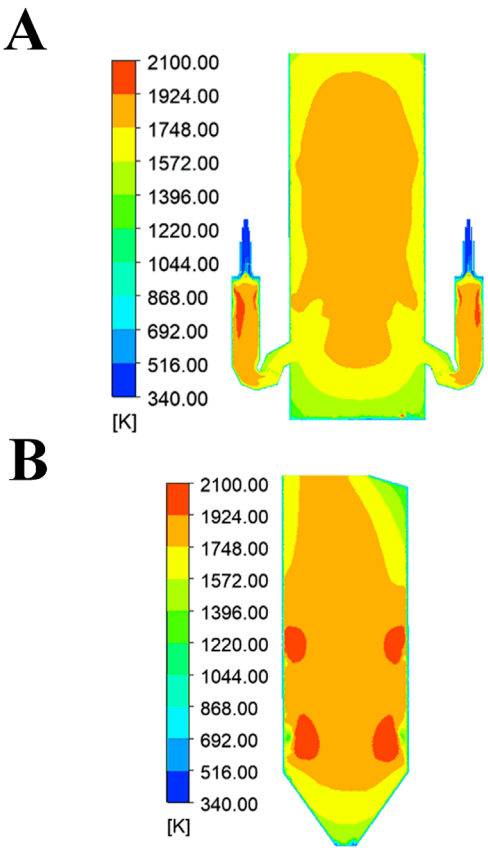

FIGURE 9
Temperature distribution in the furnace. **(A)** x = −5.4 m **(B)** y = 0 m.

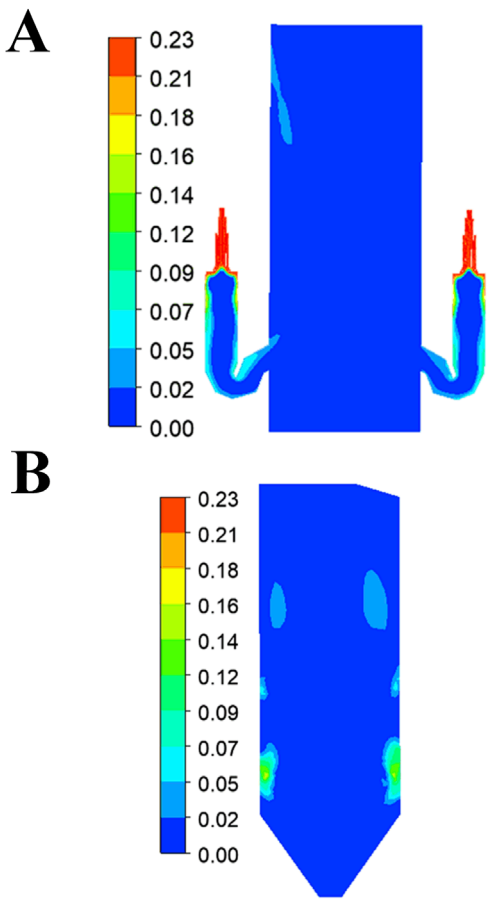

FIGURE 10
Oxygen mass fraction distribution in the furnace. **(A)** x = −5.4 m **(B)** y = 0 m.

3.4 Boundary conditions

Boundary conditions are constraints that must be satisfied on the boundaries of the computational domain during the solution process. Properly setting boundary conditions plays a crucial role in ensuring the accuracy of numerical simulation results. In boiler combustion simulations, key boundary conditions include the fluid state at inlet and outlet boundaries, the heat transfer characteristics between the wall and fluid, and the motion of pulverized coal particles upon colliding with boundaries.

In this study, mass flow inlet, fully developed flow outlet, and wall boundary conditions are employed. The air inlet boundary is configured as a mass flow inlet, with the mass flow rate for each inlet determined according to the operational air volume distribution. The outlet boundary is assigned a fully developed flow condition, with the pressure at the outlet fixed at atmospheric levels. In this configuration, the normal velocity components of all flow variables, excluding pressure, are set to zero, simulating a fully developed flow regime.

All computational domain walls are modeled as isothermal surfaces, incorporating a no-slip velocity boundary condition. The no-slip condition assumes that the tangential velocity at the wall equals the solid wall velocity, while the normal velocity

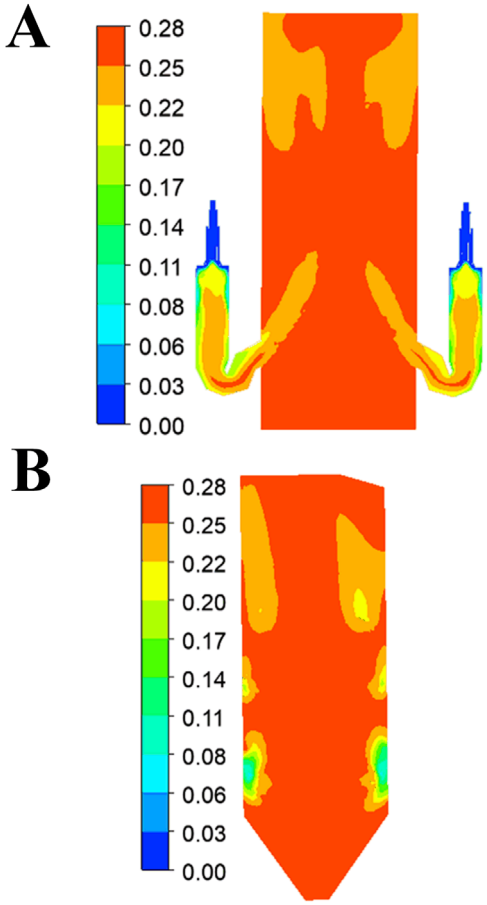

FIGURE 11
Carbon dioxide mass fraction distribution in the furnace. **(A)** x = −5.4 m **(B)** y = 0 m.

remains zero. The wall temperatures are defined in zones based on thermal calculation results, including regions such as the combustion chamber, slag trap bundle, and cooling chamber. The wall temperature in each zone is determined by averaging the inlet and outlet temperatures of the working fluid across the heating surface.

For particle boundary conditions, the outlet boundary is defined as an escape condition, where particles reaching the exit are marked as escaped and their trajectory calculations are terminated. Other wall boundaries are set to reflect conditions, meaning that when particles collide with the wall, they are reflected back into the fluid domain to continue subsequent calculations.

3.5 Working conditions

In the design conditions of this study, Naomaohu coal is burned exclusively in the combustion chamber, while the four burners operate with the original design fuel, leading to a hybrid combustion regime. The proximate and ultimate analysis data of Naomaohu coal are detailed in Table 3, with its mass fraction in the chamber fuel blend controlled at 25%. To comprehensively analyze the heat transfer characteristics of the opposed firing boiler with a slag-tap combustion chamber under the design conditions, and to investigate the influence of varying Naomaohu coal combustion ratios on the heat transfer within the furnace, three BMCR conditions are established. The corresponding operational specifications are tabulated in Table 4.

4 Results and analysis

4.1 Computational model verification

To validate the computational model, the CFD simulation results were rigorously benchmarked against thermodynamic equilibrium calculations under identical operational conditions. The thermal equilibrium model, based on energy and mass conservation principles (Zhu M. et al., 2023), computes flue gas temperatures at key furnace sections (combustion chamber, slag trap bundle, and cooling chamber) by solving coupled radiative and convective heat transfer equations (Equations 6–9).

The working condition 2 is employed for validation exercises, with quantitative comparisons between the CFD results and thermodynamic calculations detailed in Table 5. The deviations in flue gas temperature between the thermal calculations and the numerical simulations are all within an acceptable range. The largest deviation is less than 40 K. Specifically, the deviation at the combustion chamber outlet is 6.2 K, at the slag trap bundle outlet is 7.8 K, and at the cooling chamber outlet is 15.5 K. Relative to previous studies (Zhou et al., 2020), the discrepancies identified in the current work fall within acceptable limits. This confirms the precision and dependability of the proposed computational framework.

4.2 Furnace flow field characteristics analysis

Figure 6A displays the distribution of velocity vectors at the x = −5.4 m plane, intersecting the cyclone burner region of the combustion chamber. The primary and secondary airflows, guided by axial cyclone blades, generate rotational velocities of 18.4 m s^{-1} (outer secondary air) and 9.2 m s^{-1} (primary air), forming a coherent cyclonic flow pattern. This creates a localized low-pressure recirculation zone near the burner exit (Wang et al., 2020). The spatial uniformity of the flow field is evidenced by the symmetric velocity distribution across the chamber cross-section.

Figure 6B illustrates the distribution of velocity vectors at the z = −11.8 m plane, revealing symmetric flow injection from the front and rear walls. The significant horizontal velocity components develop near the burner outlets, which progressively transform into vertically dominant flow vectors with increasing downstream distance (Li et al., 2010). This systematic conversion of momentum components reflects optimized aerodynamic design, ensuring stable flame anchoring and minimizing flow separation.

An optimized flow field configuration significantly extends the residence duration of pulverized coal particles within the furnace, thereby enhancing combustion efficiency and improving heat and mass transfer characteristics. Figure 7A demonstrates the interaction of dual burner jets in the lower furnace. The high-velocity flue gas stream enters the furnace chamber along an inclined

TABLE 6 Comparison of NO_x emissions under BMCR condition (Wang et al., 2021a).

Parameter	Modular slag-tap boiler	Cyclone boiler (Wang et al., 2021a)
NO_x emissions (mg Nm^{-3})	436.7	671.4
Peak furnace temperature (K)	2140.0	2283.0

upward trajectory, generating substantial flow disturbances in the cold ash hopper section (Zhu B. et al., 2023). The interaction between dual burner jets in the lower furnace region creates a combined upward flow pattern. The cyclonic motion induced by the primary and secondary air channel blades establishes a well-defined recirculation zone near the burner outlet, which significantly extends particle residence time and promotes complete combustion reactions.

Figure 7B presents the velocity profile at y = 0 m plane. The ash hopper region exhibits intense flow disturbances caused by the impingement of combustion chamber jets. The convergence of dual burner jets in the central lower furnace generates a strong vertical flow component. The cumulative effect of multi-level burner flue gases produces a progressive velocity increase through the middle and upper furnace sections. This well-organized flow development ensures stable combustion conditions and promotes efficient gas-phase mixing throughout the furnace volume.

Figure 8 illustrates the distribution of flue gas streamlines generated by the cyclone burner within the combustion chamber. A strong cyclone forms in the upper part of the chamber, effectively carrying and mixing pulverized coal streams, promoting intense physicochemical reactions. In the lower part, the cyclone intensity gradually diminishes (Wang et al., 2021a; Yang et al., 2024). Within the slagging tube bundle area, the closely spaced tube rows generate flow disturbances that enhance the trapping of ash particles.

4.3 Furnace thermal characteristics analysis

Figure 9 delineates the thermospatial gradient characteristics across the combustion chamber domain. The central and upper zones exhibit intense pulverized coal combustion, leading to a significant thermal gradient (Zhu T. et al., 2022). The maximum temperature of approximately 2140 K is observed at the chamber's core region, corresponding to the complete combustion zone of pulverized coal. The cyclonic flow pattern establishes a distinct thermal profile characterized by elevated peripheral temperatures relative to the central region.

Thermal energy dissipation occurs progressively along the vertical axis as the flue gas undergoes convective heat transfer with the furnace walls (Qin et al., 2024). The cooling chamber's lower section demonstrates a sharp temperature reduction to approximately 1600 K, attributed to the enhanced heat exchange efficiency of the densely configured slag screen assemblies. The temperature at the flue gas outlet is around 1640 K.

The upper combustion chamber reveals four distinct thermal zones radiating from the burner nozzles' central axis. These thermal regions exhibit progressive expansion and eventual coalescence under the influence of cyclonic flow dynamics, ultimately forming a unified high-temperature zone that occupies the complete furnace volume (Wang et al., 2017). This thermal distribution pattern indicates optimized combustion efficiency and thermal field stability within the chamber.

4.4 Furnace compositional characteristics analysis

Figure 10 displays the spatial distribution of oxygen mass fraction within the furnace. Intensive oxygen consumption is observed in proximity to the burner nozzles, with the mass fraction decreasing sharply due to vigorous combustion activity. The central region, characterized by reduced gas velocities, exhibits accelerated oxygen depletion. A symmetric oxygen distribution pattern emerges, with elevated mass fractions persisting in both the central core and near-wall regions (Wang et al., 2021a; Xu et al., 2023). This phenomenon is attributed to the combined effects of enhanced flue gas velocities and moderated temperatures in these zones, which collectively decelerate the oxygen consumption rate.

The furnace chamber demonstrates near-complete oxygen depletion as the flow approaches the lowest burner cross-section. Rapid oxygen consumption in the burner vicinity leads to residual oxygen accumulation in the chamber's midsection (Wang et al., 2021b). Analysis of the coupled velocity and thermal fields indicates that this central region is characterized by reduced pulverized coal concentration, diminished temperatures, and consequently, slower reaction kinetics.

Figure 11 depicts the progressive evolution of carbon dioxide mass fraction during the combustion process. A marked increase in CO_2 concentration is detected in the vicinity of burner outlets in both the combustion and furnace chambers (Zhou et al., 2020; Zhu M. et al., 2023). The continuous elevation of CO_2 mass fraction along the flow path provides quantitative evidence of combustion completeness and the cumulative nature of gaseous product formation.

Table 6 summarizes the NO_x metrics of the retrofitted modular slag-tap boiler against the conventional cyclone boilers. The NO_x emission data for the conventional cyclone boiler was obtained from the simulation results ofWang et al. (2021a). As shown in Table 6, NO_x emissions (436.7 mg·Nm^{-3}) are 35.0% lower than cyclone systems (671.4 mg·Nm^{-3}), aligning with the reduced peak temperatures in the combustion chamber. The modular slag-tap boiler peak temperatures (2,140.0 K) are 6.3% lower than cyclone systems (2,283.0 K). NO_x emissions decreased due to optimized air staging and reduced peak combustion temperatures.

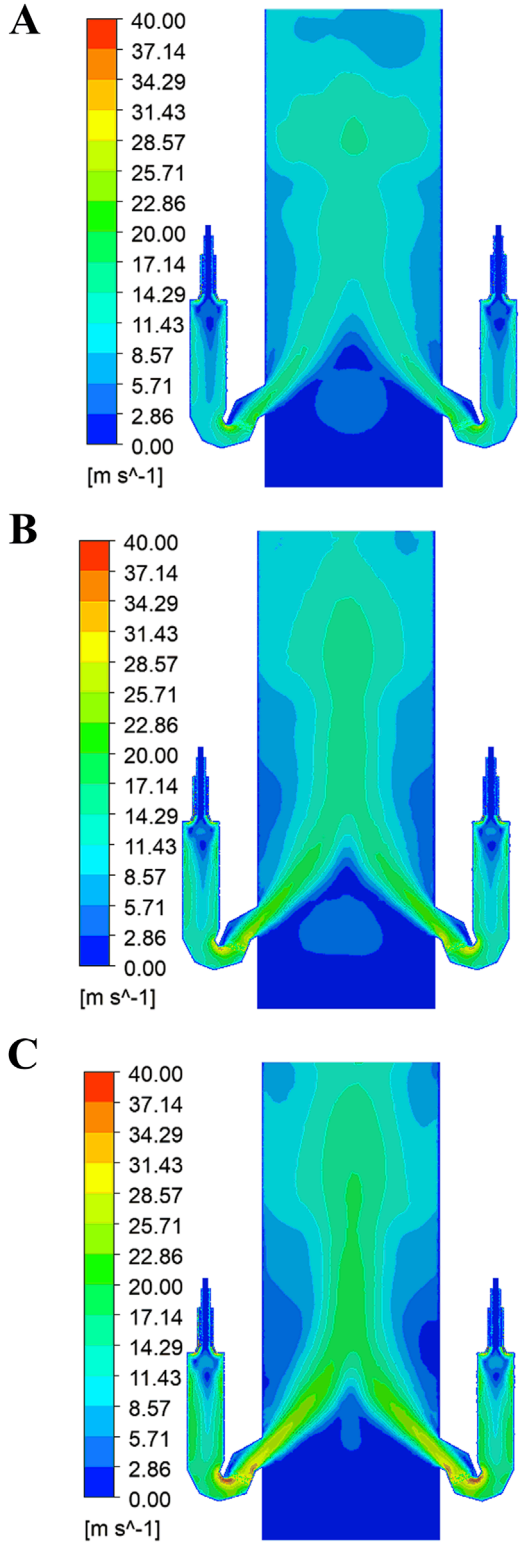

FIGURE 12
Velocity distribution in the furnace with different Naomaohu coal combustion ratios. **(A)** 20%. **(B)** 25%. **(C)** 30%.

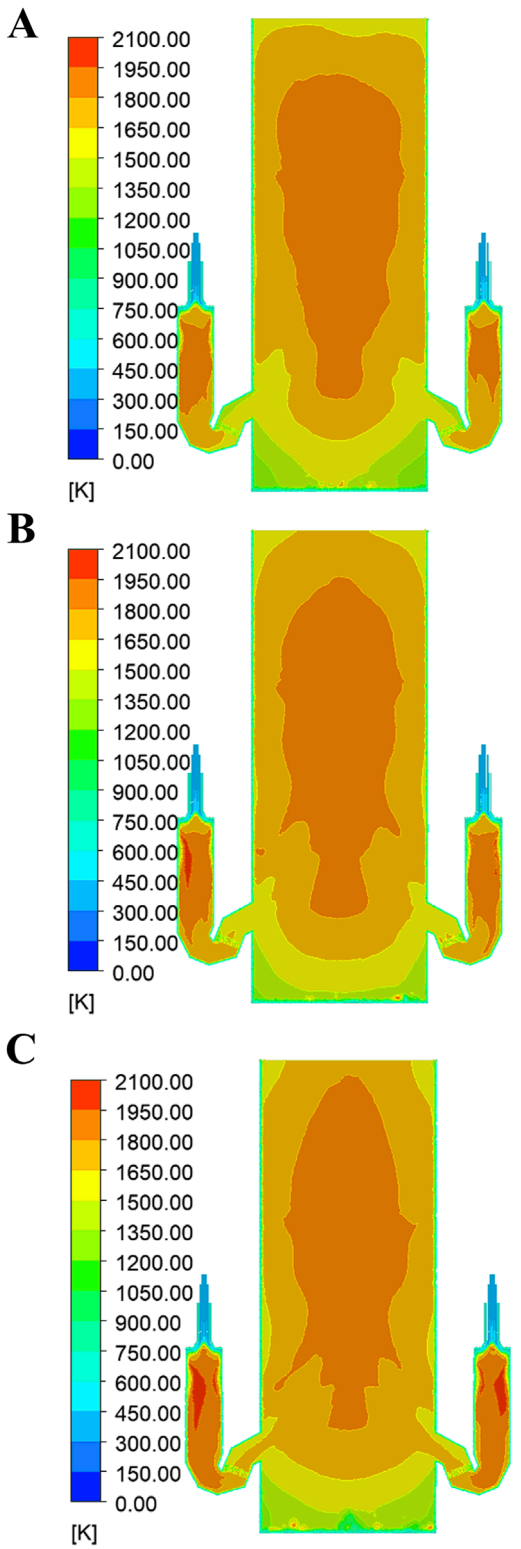

FIGURE 13
Thermal distribution in the furnace with the different Naomaohu coal combustion ratios. **(A)** 20%. **(B)** 25%. **(C)** 30%.

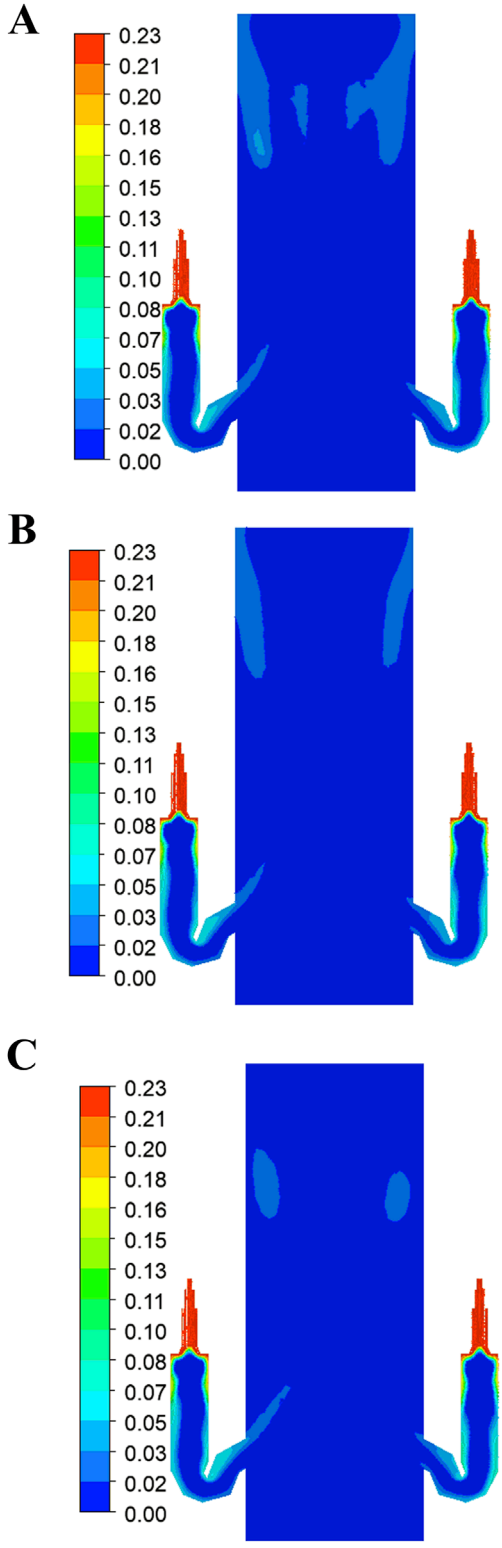

FIGURE 14
Oxygen mass fraction distribution in the furnace with different Naomaohu coal combustion ratios. **(A)** 20%. **(B)** 25%. **(C)** 30%.

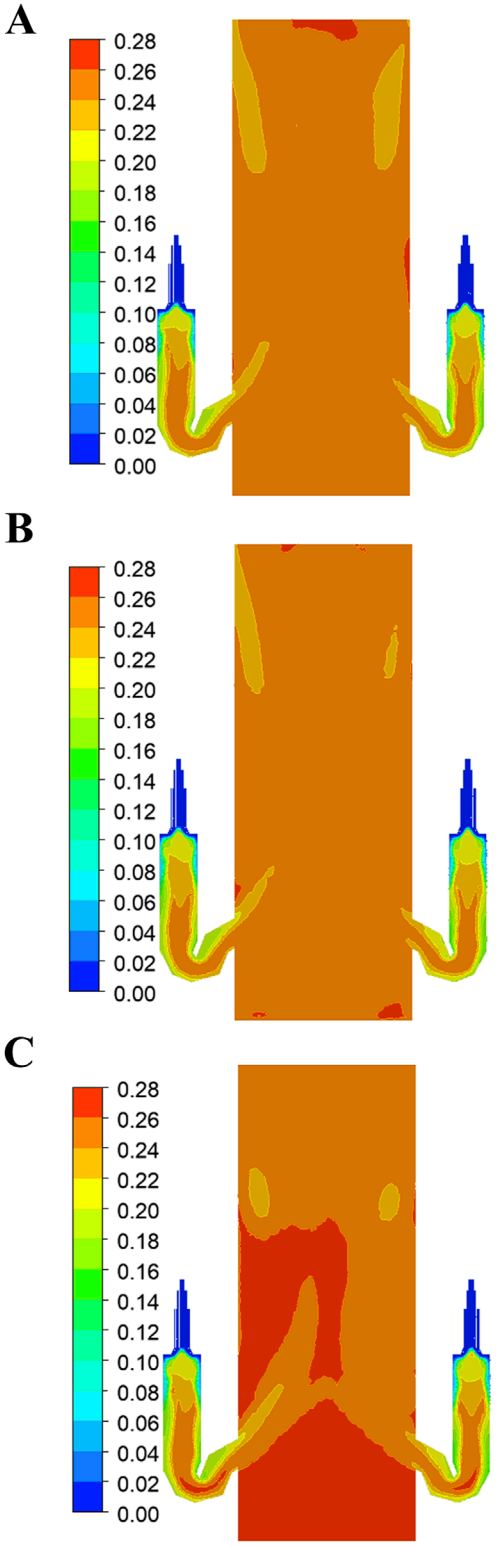

FIGURE 15
Carbon dioxide mass fraction distribution in the furnace with different Naomaohu coal combustion ratios. **(A)** 20%. **(B)** 25%. **(C)** 30%.

4.5 Impact of naomaohu coal blending proportions on thermal and mass transfer dynamics within the furnace

Figure 12 demonstrates the velocity distribution within the furnace chamber under varying Naomaohu coal combustion ratios (20%, 25%, and 30%). Progressive enhancement of the coal combustion ratio correlates with increased air distribution, particularly in the upper and middle chamber regions, accompanied by intensified cyclonic flow patterns (Yang et al., 2019; Yang et al., 2020; Zhang et al., 2020; Meng et al., 2023). The combustion chamber's elevated air distribution (approximately 50%) substantially amplifies the exit jet's influence on the furnace flow dynamics.

At higher combustion ratios, the chamber exit jet maintains its momentum over extended penetration distances. The momentum amplification of exhaust jets correlates with enhanced particle residence time, as evidenced by Lagrangian tracking of pulverized coal trajectories. This phenomenon aligns with prior studies on cyclone-driven flow optimization (Wang et al., 2021a), yet distinguishes itself through the modular retrofit design's unique capability to decouple slag capture from burner configuration. Notably, at 30% combustion ratio, the jet induces significant flow perturbations in the bottom burner region, demonstrating the exit jet's dominant role in shaping the global flow characteristics.

Figure 13 reveals the thermal distribution patterns corresponding to different Naomaohu coal combustion ratios. Increasing coal combustion percentages result in reduced furnace chamber temperatures, attributable to decreased coal feed rates, while combustion chamber temperatures exhibit an upward trend. At a 30% combustion ratio, the exit jet's strong perturbation redistributes coal particles from the bottom burner region to the chamber center, forming distinct thermal zones with a cooler region near the lower burner and a hotter core in the middle of the chamber (Liu et al., 2019; Tang et al., 2022).

Figure 14 presents the oxygen mass fraction distributions under the different combustion conditions. While the overall oxygen distribution pattern remains consistent across combustion ratios, the upper-middle chamber region exhibits reduced oxygen concentrations due to enhanced flow perturbations from the exit jet (Lv et al., 2017; Wang et al., 2021a; Xu et al., 2023). This oxygen depletion corresponds with observed velocity and temperature field characteristics, indicating intensified combustion activity in this region.

Figure 15 illustrates the progressive evolution of carbon dioxide mass fractions with increasing combustion ratios. Contrasting with oxygen distribution patterns, both the combustion chamber and upper-central furnace regions demonstrate significant CO_2 concentration increases at higher combustion ratios (Zhou et al., 2020; Zhu M. et al., 2023). This inverse relationship between oxygen depletion and CO_2 accumulation provides quantitative evidence of combustion completeness and its dependence on flow field characteristics influenced by the exit jet.

5 Conclusion

This study investigates the retrofitting of a 350 MW opposed firing boiler with a slag-tap combustion chamber to address challenges posed by Naomaohu high-alkali coal. The principal conclusions are outlined as follows:

1. The integrated slag-tap chamber improves slag capture efficiency without modifying the original slag discharge system. The modular design mitigates fouling risks and maintains combustion stability, demonstrating feasibility for retrofitting existing boilers.
2. Increasing the Naomaohu coal combustion ratio to 30% intensifies the exit jet momentum from the slag-tap chamber, redistributing coal particles toward the furnace center. While this enhances air-fuel mixing, it requires careful control of combustion intensity to maintain flow field stability and prevent operational instabilities.
3. Elevated combustion ratios create distinct a high-temperature core (~2140 K) and cooler peripheries (~1600 K), optimizing heat transfer. Oxygen depletion in the upper-middle furnace correlates with intensified reactions, whereas CO_2 accumulation in combustion zones confirms reaction completeness.
4. The retrofit framework enables efficient utilization of high-alkali coals, reduces secondary emissions, and aligns with sustainable energy objectives, offering a viable pathway for sustainable energy generation in regions reliant on high-alkali coals.

Data availability statement

The original contributions presented in the study are included in the article/supplementary material, further inquiries can be directed to the corresponding author.

Author contributions

QW: Conceptualization, Methodology, Writing – original draft. FF: Conceptualization, Data curation, Writing – review and editing. JG: Funding acquisition, Methodology, Supervision, Validation, Writing – review and editing. LZ: Funding acquisition, Supervision, Validation, Writing – original draft. YC: Formal Analysis, Investigation, Writing – review and editing. LD: Investigation, Project administration, Resources, Writing – review and editing.

Funding

The author(s) declare that financial support was received for the research and/or publication of this article. This research was funded by the project "Key Technology Development and Semi-Industrial Verification of a Slag-tap Boiler for High-Alkaline Coal in Xinjiang" (Grant No. HNKJ21-H70).

Conflict of interest

Authors QW and FF were employed by Xi'an Thermal Power Research Institute Co., Ltd.

Authors JG and LZ were employed by Harbin Boiler Co., Ltd.

The remaining authors declare that the research was conducted in the absence of any commercial or financial relationships that could be construed as a potential conflict of interest.

Generative AI statement

The author(s) declare that no Generative AI was used in the creation of this manuscript.

Publisher's note

References

Administration, C. S. (2009). Classification of coals in China (GB/T 5751-2009). *Natl. Stand. People's Repub. China, Beijing, China*. Available online at: https://std.samr.gov.cn/gb/search/gbDetailed?id=71F772D7CFE4D3A7E05397BE0A0AB82A.

Deng, J., Ran, S., Yang, Z., Fan, X., Wang, D., Guo, Y., et al. (2024). Research and application of wide load opposed firing technology for high-alkali coal fired boilers. *Therm. Power Gener.* 53 (01), 73–81. doi:10.19666/j.rlfd.202309147

Dugum, A., and Hanjalic, K. (2019). Numerical simulation of coal-air mixture flow in a real double-swirl burner and implications on combustion anomalies in a utility boiler. *Energy* 170, 942–953. doi:10.1016/j.energy.2018.12.121

Gong, Y., Fu, P., Liu, Y., and Bie, K. (2021). Sintering characteristics of Zhundong coal ash and refractory material of slag tap pulverized coal boiler. *J. Combust. Sci. Technol.* 27 (1), 67–73. doi:10.11715/rskxjs.R201912003

Hang, Y., Jin, J., Yang, H., Zhang, R., Zhu, Y., and Liu, Z. (2020). Experimental study on combustion characteristics of Zhundong coal. *J. Chin. Soc. Power Eng.* 40 (03), 185–190+212. doi:10.19805/j.cnki.jcspe.2020.03.002

Hariana, P. A., Prabowo, Hilmawan, E., Darmawan, A., and Aziz, M. (2023). Effectiveness of different additives on slagging and fouling tendencies of blended coal. *J. Energy Inst.* 107, 101192. doi:10.1016/j.joei.2023.101192

Huang, D., Zhang, S., Chang, M., Shi, Y., Lin, C., Xu, J., et al. (2021). Research progress on sintering characteristics of high sodium coal ash. *Clean. Coal Technol.* 27 (01), 83–94. doi:10.13226/j.issn.1006-6772.A20111603

Huang, S., Zhang, L., Yan, J., Wang, Z., Lei, Z., Li, Z., et al. (2022). Investigation on cofiring high-alkali coal with coal gangues: SO2, NO reduction and ash slagging inhibition. *CIESC J.* 73 (12), 5581–5591. doi:10.11949/0438-1157.20221221

International, A. (2019). *Standard classification of coals by rank (ASTM d388-19)*. West Conshohocken, PA, USA: ASTM International.

Jing, X. H., Pu, Y., Li, Z. Y., Tang, Q. L., Yao, B., Fu, P. F., et al. (2022). Experimental investigation of gaseous sodium release in slag-tapping coal-fired furnaces by spontaneous emission spectroscopy. *Energies* 15 (11), 4165. doi:10.3390/en15114165

Lei, Y., Fu, P., Tang, S., Yue, F., Bie, K., and Liu, Y. (2019). Occurrence form of sodium in Zhundong coal and its evaporation and condensation characteristics. *J. Combust. Sci. Technol.* 25 (2), 124–130. doi:10.11715/rskxjs.R201807004

Li, G., Wang, C. A., Wang, P., Du, Y., Liu, X., Chen, W., et al. (2017). Ash deposition and alkali metal migration during Zhundong high-alkali coal gasification. *Energy Procedia* 105, 1350–1355. doi:10.1016/j.egypro.2017.03.497

Li, G. Y., Wang, C. A., Yan, Y., Jin, X., Liu, Y. H., and Che, D. F. (2016). Release and transformation of sodium during combustion of Zhundong coals. *J. Energy Inst.* 89 (1), 48–56. doi:10.1016/j.joei.2015.01.011

Li, X., Li, J., Wu, G. G., Bai, Z. Q., and Li, W. (2018). Clean and efficient utilization of sodium-rich Zhundong coals in China: behaviors of sodium species during thermal conversion processes. *Fuel* 218, 162–173. doi:10.1016/j.fuel.2018.01.027

Li, X. Y., Li, G. Y., Cao, Z. D., and Xu, S. S. (2010). Research on flow characteristics of slag film in a slag tapping gasifier. *Energy and Fuels* 24 (9), 5109–5115. doi:10.1021/ef100197k

Li, Y. D., Yang, D., Zhou, X. H., Dong, L., Suo, L. H., and Sun, W. B. (2022). Heavy metal migration characteristics of co-combustion between sewage sludge and high alkaline coal on circulating fluidized bed. *J. Therm. Sci.* 31 (6), 2178–2188. doi:10.1007/s11630-022-1695-5

Liu, Y. Q., Cheng, L. M., Ji, J. Q., and Zhang, W. G. (2019). Ash deposition behavior in co-combusting high-alkali coal and bituminous coal in a circulating fluidized bed. *Appl. Therm. Eng.* 149, 520–527. doi:10.1016/j.applthermaleng.2018.12.080

Lv, H., Tong, J., Qi, X., and Hua, G. (2017). Numerical simulation on air flow distribution characteristics for 1 000 MW swirl burners. *J. Eng. Therm. Energy Power* 32 (1), 86–90. doi:10.16146/j.cnki.rndlgc.2017.01.0015

Meng, Y., Li, Y., Yang, Z., Qi, Q., Jiang, T., Zhao, X., et al. (2023). Adaptability research of different types of boiler burning Naomaohu high-alkali coal in one power plant. *Therm. Power Gener.* 52 (7), 142–149. doi:10.19666/j.rlfd.202212295

Nakamura, H., Zhang, J. W., Hirose, K., Shimoyama, K., Ito, T., and Kanaumi, T. (2023). Generating simplified ammonia reaction model using genetic algorithm and its integration into numerical combustion simulation of 1 MW test facility. *Appl. Energy Combust. Sci.* 15, 100187. doi:10.1016/j.jaecs.2023.100187

Ni, Y. G., Hu, S. H., Meng, H. X., Wang, J. K., Li, H., Zhou, H., et al. (2022). Experimental research on fully burning high-alkali coal in a 300 MW boiler with slag-tap furnace. *Asia-Pacific J. Chem. Eng.* 17 (5). doi:10.1002/apj.2807

Qi, Q., Ma, S., Yang, Z., Li, Y., Jia, Z., and Lu, H. (2024). Study on corrosion prevention and control of the furnace of a 350 MW opposite-firing boiler burning high-alkali coal. *Therm. Power Gener.* 53 (01), 91–98. doi:10.19666/j.rlfd.202306086

Qin, S., Du, J., Li, C., and Zhou, Y. (2024). Numerical investigations on the aerodynamics and flue gas recirculation optimization of cyclone-fired coal boiler. *Therm. Power Gener.* 53 (1), 53–63. doi:10.19666/j.rlfd.202307108

Rachele, L., Cristiana, B., Marco, F., Leonardo, T., and Chiara, G. (2023). Impact of H2-enriched natural gas on pollutant emissions from domestic condensing boilers: numerical simulations of the combustion chamber. *Int. J. Hydrogen Energy* 48 (51), 19686–19699. doi:10.1016/j.ijhydene.2023.02.040

Shen, Z. J., Hua, X., Liang, Q. F., Xu, J. L., Han, D., and Liu, H. F. (2017). Reaction, crystallization and element migration in coal slag melt during isothermal molten process. *Fuel* 191, 221–229. doi:10.1016/j.fuel.2016.11.048

Shi, S., Fu, C., Sui, H., and Liang, S. (2023). Standard methods of boiler thermodynamic calculation. *Clean. Coal Technol.* 29 (S2), 370–376. doi:10.13226/j.issn.1006-6772.22103102

Song, W., and Li, M. (2022). Study on slagging and contamination test of high alkali coal combustion and targeted operation measures of boiler. *Coal Sci. and Technol. Mag.* 43 (06), 75–78+85. doi:10.19896/j.cnki.mtkj.2022.06.017

Su, X. Q., Fang, Q. Y., Ma, L., Zhang, C., Chen, G., Yin, C. E., et al. (2024). Efficient and low-NO combustion in a grate-fired boiler by feeding biomass non-uniformly along grate width: an integrated modeling study with experimental validation. *Energy* 312, 133583. doi:10.1016/j.energy.2024.133583

Tang, C. W., Pan, W. G., Zhang, J. K., Wang, W. H., and Sun, X. L. (2022). A comprehensive review on efficient utilization methods of High-alkali coals combustion in boilers. *Fuel* 316, 123269. doi:10.1016/j.fuel.2022.123269

Wang, C. A., Li, G. Y., Du, Y. B., Yan, Y., Li, H., and Che, D. F. (2018). Ash deposition and sodium migration behaviors during combustion of Zhundong coals in a drop tube furnace. *J. Energy Inst.* 91 (2), 251–261. doi:10.1016/j.joei.2016.11.010

Wang, H., Ma, X., Deng, L., Bai, P., and Wang, Y. (2024). Double-U-shaped low-nitrogen combustion system of liquid slag discharging boiler containing classified furnace smoke.

Wang, W., Huang, Z., Fang, F., and Liao, Y. (2021). Effect of primary air blade inclination angle on combustion and NOx emission of a cyclone boiler with slag-tap furnace. *J. Chin. Soc. Power Eng.* 41 (1), 8–13. doi:10.19805/j.cnki.jcspe.2021.01.002

Wang, W., Luo, X., Yang, Z., and Liao, Y. (2021). Effect of excess air coefficient on combustion and NOx emission of cyclone boiler with pure high alkali coal. *J. Eng. Therm. Energy Power* 36 (04), 73–79. doi:10.16146/j.cnki.rndlgc.2021.04.011

Wang, W., Tian, M., Hu, Q., and Zheng, M. (2017). Numerical simulation of gas-solid two-phase flowing in opposed firing supercritical boiler. *J. Eng. Therm. Energy Power* 32 (5), 64. doi:10.16146/j.cnki.rndlgc.2017.05.011

Wang, W. S., Sun, Y. Z., Huang, Z. H., Liao, Y. H., and Fang, F. (2020). Numerical simulation of NO_x emission characteristics of a cyclone boiler with slag-tap furnace. *Acs Omega* 5 (46), 29978–29987. doi:10.1021/acsomega.0c04367

Wang, Y. A., Zou, L., Shao, H. S., Bai, Y. Y., Liu, Y., Zhao, Q. X., et al. (2022). Co-combustion of high alkali coal with municipal sludge: thermal behaviour, kinetic analysis, and micro characteristic. *Sci. Total Environ.* 838, 156489. doi:10.1016/j.scitotenv.2022.156489

Wu, Q., Hu, S., Liu, J., Zhang, Y., Li, H., and Zhou, H. (2024). Slagging and element migration characteristics of Zhundong coal in horizontal liquid slag cyclone furnace. *Clean. Coal Technol.* 30 (6), 27–35. doi:10.13226/j.issn.1006-6772.XJ24052901

Xu, C., Shao, Y., Lu, P., and Song, T. (2023). Numerical simulation of low NOx swirl combustor with inverse diffusion flame. *J. Eng. Therm. Energy Power* 38 (5), 170–178. doi:10.16146/j.cnki.rndlgc.2023.05.021

Xu, T. (2024). Migration and transformation characteristics of Na in high-alkali coal combustion under liquid slagging condition. *Shanxi Electr. Power (04)*, 46–51.

Yang, J., Wang, J., Ma, X., Deng, L., Da, Y., and Che, D. (2024). Thermal calculation and numerical simulation on double-U flame slag-tap boiler that fully burning high-alkali coal. *Therm. Power Gener.* 53 (1), 38–45. doi:10.19666/j.rlfd.202309154

Yang, Y., Chen, C., Chen, X., Wang, D., and Yao, B. (2019). Experimental study on fouling characteristics for blending ratio of high alkali coal in Hami area. *Coal Sci. Technol.* 47 (5), 214–219. doi:10.13199/j.cnki.cst.2019.05.034

Yang, Y., Wang, D., Chen, X., and Yao, B. (2020). Study on comprehensive evaluation of slagging characteristics of high-alkali coal blending combustion from Hami Area. *Coal Sci. Technol.* 48 (6), 207–213. doi:10.13199/j.cnki.cst.2020.06.027

Zhang, P., Lyu, J., Wang, H., Xin, S., Liang, J., Wu, W., et al. (2020). Study kaolin on operation characteristics of a 300 MW CFB boiler burning Zhundong high-alkali coal. *Boil. Technol.* 51 (04), 29–32+54.

Zhang, X., Wang, Z., Zhou, G., Guo, Y., Yang, Z., and Yao, W. (2023). Present situation and prospect of high alkali coal combustion technology in power plant boiler. *Therm. Power Gener.* 52 (07), 133–141. doi:10.19666/j.rlfd.202305079

Zhang, X., Wu, X., and Chen, N. (2016). Experimental study on Xinjiang high-alkali ash deposition and slagging behavior in a 3MWth pilot-scale test facility. *Boil. Technol.* 47 (04), 44–47.

Zhou, H., Li, H., Ma, X., Li, D., Zhang, H., Liu, X., et al. (2024). Operational optimization on fully burning and high proportion blend burning high-alkali coal in boiler with slag-tap furnace. *Therm. Power Gener.* 53 (1), 64–72. doi:10.19666/j.rlfd.202309162

Zhou, J., Zhu, M., Su, S., Chen, L., Xu, J., Hu, S., et al. (2020). Numerical analysis and modified thermodynamic calculation methods for the furnace in the 1000 MW supercritical CO2 coal-fired boiler. *Energy* 212, 118735. doi:10.1016/j.energy.2020.118735

Zhu, B., Shang, B. C., Guo, X., Wu, C., Chen, X. Q., and Zhao, L. L. (2023). Study on combustion characteristics and NOx formation in 600 MW coal-fired boiler based on numerical simulation. *Energies* 16 (1), 262. doi:10.3390/en16010262

Zhu, J., Ran, S., Pan, S., Yi, G., Liu, W., Tang, Z., et al. (2022). Research and development of the first 660 MW ultra-supercritical opposed firing boiler with fully fired Zhundong high alkali coal. *Power Equip.* 36 (03), 182–188. doi:10.19806/j.cnki.fdsb.2022.03.007

Zhu, M., Chen, L., Zhou, L. A., Jiang, L., Su, S., Hu, S., et al. (2023). Experimental test, numerical analysis and thermal calculation modeling of hundreds kWth-class supercritical CO2 fossil-fired boiler system. *Energy* 284, 128523. doi:10.1016/j.energy.2023.128523

Zhu, T., Tang, C. L., Ning, X., Wang, L. M., Deng, L., and Che, D. F. (2022). Experimental study on NO emission characteristics of Zhundong coal in cyclone furnace. *Fuel* 311, 122536. doi:10.1016/j.fuel.2021.122536